energy&fuels

Fossil Fuels

Combining Image Recognition and Simulation to Reproduce the Adsorption/Desorption Behaviors of Shale Gas

Kui Lin, Xianfu Huang, and Yapu Zhao

Just Accepted

Combining Image Recognition and Simulation to Reproduce the Adsorption/Desorption Behaviors of Shale Gas

Kui Lin,[†,‡] Xianfu Huang,[†,‡] and Ya-Pu Zhao[*,†,‡]

ABSTRACT: Shale gas stored in deep shale is in a supercritical state. Therefore, it is necessary to study the adsorption and desorption properties of supercritical shale gas. To accurately determine the state of methane (CH_4) in the pores of deep shale, the fractal characteristics of several shale samples drilled at 2650 m depth are analyzed using scanning electron microscopy (SEM) and image analysis. We find nanopores with different fractal features in the shale. The effects of adsorption energy and substrate strain on adsorption capacity are clarified. The virial coefficients of CH_4 are obtained by molecular dynamics (MD) simulations and are consistent with the experiment. The adsorption and desorption of CH_4 in different fractal nanopores are modeled using grand canonical Monte Carlo (GCMC) simulations at different temperatures and pressures (from capillary condensation to supercritical state). Additionally, the gas-in-place (GIP), excess adsorption and absolute adsorption isotherms are obtained. We find the crossover of excess adsorption isotherms, which was observed in the experiment, and the absolute adsorption amount increases with the increase in pressure in the case of ultrahigh pressure (> 40 MPa). Moreover, we obtain an ultrahigh pressure dual-site Langmuir equation and it can accurately describe observed adsorption isotherms from low pressure to ultrahigh pressure. Our study visually reproduces the adsorption/desorption behaviors of CH_4 under *in situ* conditions in deep shale and reveals their microscopic mechanism.

KEYWORDS: *shale gas; supercritical adsorption/desorption; fractal characteristics; in situ pores; simulations*

†State Key Laboratory of Nonlinear Mechanics, Institute of Mechanics, Chinese Academy of

Sciences, Beijing 100190, China.

‡School of Engineering Science, University of Chinese Academy of Sciences, Beijing 100049, China

*Correspondence and requests for materials should be addressed to Y. –P. Zhao (email: yzhao@imech.ac.cn)

1

1. INTRODUCTION

Shale gas is an unconventional energy source with abundant reserves[1-2]. It has been a major component of the hydrocarbon economy and will continue to play a significant role[3]. To extract shale gas, various mining technologies, such as horizontal drilling, hydraulic fracturing and supercritical carbon dioxide fracturing, have been developed[4-5]. Shale gas has been successfully exploited in the United States, and its production reached ~ 40% of total natural gas production in 2013[6]. Other countries, such as China, the United Kingdom, Argentina and Mexico, have also begun to exploit shale gas[7]. Shale gas primarily consists of methane (CH_4) and is stored in shale hundreds of meters to several kilometers deep[8]. The occurrence state of shale gas mainly includes the dissolved state, the free state and the adsorption state, depending on the pore structure and formation conditions (e.g., pressure, temperature)[9-11]. However, the storage characteristics of shale gas are complicated as a result of changes in stratigraphic structure. In addition, it is difficult for one mining method to be effectively applied to all storage conditions[12-14]. To maximize efficiency and economic benefits, it is necessary to have a precise understanding of the storage characteristics of shale gas and estimate its true reserves.

The multiscale pore structure and its distribution in shale have been studied by experiment[15-19]. Such studies indicate that the characteristic pore length in kerogen is 20 ~ 100 nm, whereas in mineral, it is 10 ~ 1000 nm. Most CH_4 is adsorbed on the surface of pores by the weak van der Waals force[1]. The gas in the pores is difficult to desorb, which seriously affects exploitation efficiency. Therefore, the adsorption and thermodynamic properties of CH_4 in nanopores have been investigated by molecular dynamics (MD) simulations[20-23]. In addition, the displacement and transport behaviors of CH_4 in the pores by multiple supercritical fluids have been studied by simulations[24-28]. In experiments, the thermodynamic properties of high pressure (up to 27 MPa) CH_4 adsorption in shale have been investigated, and the dual-site Langmuir equation for estimating high-pressure shale gas resources has been obtained[6, 29]. However, to determine the characteristics of shale gas storage, a simulation can more easily model real conditions and is more economical than an experiment. In particular, the pressure condition can reach ultrahigh pressure (> 40 MPa). Most simulation models are simple pore models of a single structure composed of graphene, carbon nanotubes or other materials[21, 30-32]. Fractal geometry can effectively characterize pore heterogeneity and surface roughness and has been widely used in

2

pore analysis of coal and shale[33-34]. Although the structural characteristics of shale have been extensively studied[35-36], there are few MD simulation studies on the adsorption of CH_4 in porous media, particularly in *in situ* structures. Modeling based on *in situ* structures can be used to visually and realistically understand the adsorption properties in deep shale on the atomic level.

In this paper, we determine the *in situ* pore structure by scanning electron microscopy (SEM) observation of several shale samples from 2650 m deep and the fractal characteristics of the pores through images analysis. As a heterogeneous material, the pores of different components in shale have different fractal characteristics. Then, we construct a molecular dynamics (MD) simulation model with an *in situ* structure. First, we obtain the virial coefficients of CH_4 to achieve the conversion between fugacity and pressure and compare it experimentally. We investigate the adsorption and desorption progresses of CH_4 in fractal nanopores from negative pressure to ultrahigh pressure (i.e., 0.1 MPa ~ 50 MPa) at different temperatures (i.e., 150 K, 180 K, 210 K, 300 K, 320 K, 340 K and 360 K) using grand canonical Monte Carlo (GCMC) simulations. From these simulations, we find capillary condensation and supercritical adsorption phenomena of CH_4 in nanopores. The gas-in-place (GIP), excess adsorption and absolute adsorption isotherms are clarified. We discover the crossover of excess adsorption isotherms, which has been observed experimentally, and find that the absolute adsorption amount increases with the increase in pressure in the case of ultrahigh pressure (> 40 MPa). We obtain an ultrahigh pressure dual-site Langmuir equation and it is a good description of the adsorption behavior from low pressure to ultrahigh pressure. In addition, the desorption hysteresis loop appears at low temperatures but hardly exists in the supercritical state. Finally, the radial distribution function of CH_4 in nanopores under different conditions is compared and analyzed. Our study visually reproduces the state of CH_4 in deep shale and reveals the mechanism of adsorption/desorption at the atomic scale.

2. METHODS

2.1. SEM Analysis of Shale Samples. Shale samples were collected at a depth of 2650 m in the Chang 7 shale of Yanchang formation, Huanxian-Shangliyuan area, Ordos Basin, China. According to Cui et al. (2019)[37], Shangliyuan area is high maturity and deep buried shale gas area with high total organic content (TOC > 6%) and the Ro > 1%. In addition, more detailed and comprehensive studies have been made on the geological background of Southwest Ordos Basin[38].

3

Super-resolved field–emission scanning electron microscopy (FE-SEM) was used to observe the pore structure of the shale samples. The sample size for the SEM scanning was $10\,\text{mm} \times 15\,\text{mm} \times 5\,\text{mm}$. To preserve the original nanopores of the samples, we adopted the ion beam milling technique after polishing. The surface of the shale sample was bombarded with accelerated argon ions, making the surface extremely smooth and retaining the true pore profile.

2.2. Image Analysis. After obtaining the SEM images of the shale samples, we programmatically identified the grayscale of the images, digitized the pore structure, and then analyzed the pore structure. The binary images of the samples were analyzed by the box-counting method to obtain the fractal dimension of the pores in different components of the shale.

2.3. Molecular Dynamics Simulations. MD simulations implemented in LAMMPS[39] were performed to investigate the compressibility factor of CH_4 and then to obtain the fugacity coefficients. The Lennard-Jones (LJ) potential[40] was used to describe the interactions between particles $E_{ij} = 4\varepsilon_{ij}\left[\left(\sigma_{ij}/r_{ij}\right)^{12} - \left(\sigma_{ij}/r_{ij}\right)^{6}\right]$, where ε_{ij} is the LJ potential well depth, σ_{ij} is the zero-potential distance and r_{ij} is the distance between particle i and j. To simplify the large-scale simulations, the coarse-grained model was used. The molecular structure of CH_4 was ignored and treated as an LJ particle. The LJ parameters were obtained by consistent valence force field (CVFF)[41], with $\sigma = 0.3751\,\text{nm}$ and $\varepsilon = 0.294\,\text{kcal}\cdot\text{mol}^{-1}$. The constant number of atoms, pressure and temperature (*NPT*) ensemble was used with the Nose/Hoover method to regulate the temperature at 300 K, 320 K, 340 K and 360 K. Each pressure relaxes for 0.1 ns with time step 1 fs.

We constructed a 3D porous model based on the *in situ* pore structure images obtained by SEM. The structure consists of uniformly arranged LJ particles separated by 2 Å. According to the potential parameters of the adsorbent used in the simulation of shale adsorption in previous studies[30], the LJ parameters of the pore structure were $\sigma' = 0.36\,\text{nm}$ and $\varepsilon' = 0.148\,\text{kcal}\cdot\text{mol}^{-1}$. The values of potential parameters between two elements were calculated by the Lorentz-Berthelot (LB) rule: $\sigma_{ij} = \left(\sigma_i + \sigma_j\right)/2,\ \varepsilon_{ij} = \sqrt{\varepsilon_i \cdot \varepsilon_j}$. The GCMC method[42] was used to investigate the adsorption and desorption of CH_4 in the porous media. The grand canonical ensemble means that when the system is equilibrium, the chemical potentials μ between phases are equal at temperature *T*. We calculated the adsorption and desorption behavior of CH_4 in three

4

porous media with different fractal dimensions at different temperatures (150 K, 180 K, 210 K, 300 K, 320 K, 340 K and 360 K) and fugacities (0.1 MP ~ 36 MPa), and performed 10000 runs for equilibrium in each stage with a time step of 1 fs. All simulations were done in 60 core parallel computations. The calculation time depends on the size and condition of the model. For model I, each data point takes about 3200 seconds at a temperature of 340 K.

3. RESULTS AND DISCUSSION

3.1. Fractal Dimension of Shale Pores. From the SEM shale samples images, we find that the pores have different characteristics in different components. Figs 1a-d show the pores in kerogen, the pores in mineral, the pores in the clay, and the distribution of the kerogen in the shale, respectively. Binary images that correspond to the SEM images are show in Figs. 1e-h. Using a binary image, we can further analyze the fractal dimension of the pore structure. In this study, the box-counting method is used to compute the pore distribution fractal dimension. As shown in Figs. 1i-l, by covering a box of length δ on the binary image, the fractal dimension is calculated by[43]

$$D = -\lim_{\delta \to 0} \frac{\ln(N(\delta))}{\ln(\delta)}, \tag{1}$$

where $N(\delta)$ is the number of boxes required to completely cover the white area. It can also be written as follows:

$$\ln(N(\delta)) = -D\ln(\delta) + \text{constant} . \tag{2}$$

Thus, we can obtain the fractal dimension from the slope of the linear fitting. The fractal dimension calculation results for the corresponding structure are shown in Fig. 2. All of the plots display good fits ($R^2 > 0.99$). For the calculation results for additional shale samples, please see Table s1 and Fig. S1 in the supplementary materials. It can be observed from the results that the fractal dimension of pores has regularity: pores in kerogen > kerogen in clay > pores in minerals > pores in clay. The larger that the fractal dimension is, the rougher the boundary is.

3.2. Effect of Substrate Properties on Adsorption. After obtaining the porous structure by SEM, to select the appropriate model to simulate the actual adsorption, the choice of the geometric properties of the substrate and the potential parameters is important. Therefore, it is necessary to investigate the effect of the substrate on adsorption. The Hamiltonian of 2D motion of the

5

adsorbed molecular on the substrate includes kinetic energy and potential energy:

$$H(q, p) = \frac{p^2}{2m} + E_{\mathrm{a}},$$ (3)

where m is the relative molecular mass, E_{a} is the potential energy which is equal to the adsorption energy, q is the generalized coordinates and p is the generalized momentum. According to the grand canonical partition function:

$$\begin{aligned}
\Xi &= \sum_{N=0}^{\infty} \frac{\exp(-N\alpha)}{N!h^{2N}} \int \exp\left[-\beta H(q, p)\right] \mathrm{d}\Omega \\
&= \sum_{N=0}^{\infty} \frac{\exp(-N\alpha)}{N!h^{2N}} \int \cdots \int \exp\left[-\beta H(q, p)\right] \mathrm{d}q_1 \cdots \mathrm{d}q_{2N} \mathrm{d}p_1 \cdots \mathrm{d}p_{2N}
\end{aligned}$$ (4)

where $\alpha = -\mu/(k_{\mathrm{B}}T)$, $\beta = 1/(k_{\mathrm{B}}T)$, μ is the chemical potential, k_{B} is the Boltzmann constant, T is the specified temperature, N is the number of adsorbed molecules, h is the Planck constant and Ω is the number of microstates. The partition function of a single adsorbed molecule is as follows:

$$\begin{aligned}
Z_1 &= \frac{1}{h^2} \iint \mathrm{d}q_1 \mathrm{d}q_2 \iint \exp\left[-\beta H(q, p)\right] \mathrm{d}p_1 \mathrm{d}p_2 \\
&= \frac{1}{h^2} \iint \mathrm{d}x\mathrm{d}y \iint \exp\left[-\beta\left(p_{\mathrm{x}}^2 + p_{\mathrm{y}}^2\right)\big/2m - \beta E_{\mathrm{a}}\right] \mathrm{d}p_{\mathrm{x}} \mathrm{d}p_{\mathrm{y}}, \\
&= \frac{2\pi m k_{\mathrm{B}} T A}{h^2} \exp(-\beta E_{\mathrm{a}})
\end{aligned}$$ (5)

where A is the surface area. Combining equations (4) and (5), we have

$$\begin{aligned}
\Xi &= \sum_{N=0}^{\infty} \frac{\exp(-N\alpha)}{N!} \left[\frac{2\pi m k_{\mathrm{B}} T A}{h^2} \exp(-\beta E_{\mathrm{a}})\right]^N \\
&= \sum_{N=0}^{\infty} \frac{1}{N!} \left[\frac{2\pi m k_{\mathrm{B}} T A}{h^2} \exp(-\alpha - \beta E_{\mathrm{a}})\right]^N \\
&= \exp\left[\frac{2\pi m k_{\mathrm{B}} T A}{h^2} \exp(-\alpha - \beta E_{\mathrm{a}})\right]
\end{aligned}$$ (6)

Therefore, the average number of molecules adsorbed can be calculated by

$$\overline{N_{\mathrm{a}}} = -\frac{\partial}{\partial \alpha} \ln \Xi = \frac{2\pi m A}{\beta h^2} \exp(-\alpha - \beta E_{\mathrm{a}}).$$ (7)

Assuming that the substrate is uniformly deformed, according to the Cauchy-Born rule[44], the lattice vectors before and after the deformation can be connected by deformation gradient $\boldsymbol{F}$:

$$\boldsymbol{a} = \boldsymbol{F} \cdot \boldsymbol{A} = \frac{\partial \boldsymbol{x}}{\partial \boldsymbol{X}} \cdot \boldsymbol{A},$$ (8)

where $\boldsymbol{A}$ and $\boldsymbol{a}$ are lattice vectors before and after deformation, respectively. $\boldsymbol{x}(\boldsymbol{X}, t)$ can

6

denote the deformation function, which relates the points X in a reference configuration Ω_0

to the points $x = x(X,t)$ in the current configuration Ω_t. Adsorption energy is a function of

lattice constant. Therefore, the adsorption energy before and after deformation can be written as

$E_a = \varphi(A)$ and $E_a' = \varphi(a) = \varphi(F \cdot A)$, respectively. Thus, the average number of adsorbed

molecules after deformation is as follows:

$$\overline{N_a'} = A(F \cdot A)\frac{2\pi m}{\beta h^2}\exp\left[-\alpha - \beta\varphi(F \cdot A)\right]. \tag{9}$$

In homogeneous deformation, the symmetric displacement gradient H is identical to the

Cauchy strain tensor ε:

$$\varepsilon \equiv \frac{1}{2}\left(H + H^T\right) = H = \frac{\partial x}{\partial X} - I. \tag{10}$$

For uniaxial strain conditions, as shown in Fig. 3a, the substrate deformation only occurs in

one direction, while no deformation occurs in the other two directions. Assuming that the axial

strain is ε. Then, the deformation gradient is:

$$F = H + I = \begin{bmatrix} \varepsilon+1 & 0 & 0 \\ 0 & 1 & 0 \\ 0 & 0 & 1 \end{bmatrix}. \tag{11}$$

In this case, $A(F \cdot A) = A \cdot \frac{\partial x}{\partial X} = A(\varepsilon+1)$ and $\varphi(F \cdot A) \propto \frac{1}{A(F \cdot A)} = \frac{1}{A(\varepsilon+1)}$. Hence, the

ratio of deformation to original adsorption is expressed as follows:

$$\begin{cases} \overline{N_a'}/\overline{N_a} = (1+\varepsilon)\exp\left(\beta E_a \frac{\varepsilon}{1+\varepsilon}\right) & \text{total} \\ \overline{N_a'}/\overline{N_a} = \exp\left(\beta E_a \frac{\varepsilon}{1+\varepsilon}\right) & \text{unit area} \end{cases} \tag{12}$$

Figs. 3c,d show the effects of strain and adsorption energy on the total adsorption capacity of

the substrate and the adsorption capacity per unit area, respectively. The compressive stress

increases the adsorption capacity, while the tensile stress reduces the adsorption capacity. On the

atomic scale, strain is the change of the relative position of atoms. Thus, by clarifying the effect of

substrate strain (or atomic distribution) and adsorption energy on adsorption capacity, a more

practical adsorption model can be designed.

3.3. MD Simulation Models with an *in situ* Pore Structure. According to the SEM images

of three pore structures (i.e., pores in kerogen, pores in minerals, pores in clay), the corresponding

7

three-dimensional (3D) simulation models were constructed (Fig. 4) and named as models I, II and III. The sizes of models I, II and III are $44.8 \times 44.8 \times 3.5\,\text{nm}$, $80.0 \times 80.0 \times 3.5\,\text{nm}$ and $62.4 \times 62.4 \times 3.5\,\text{nm}$, respectively. The SEM images are 2D. Here, we extend directly in the direction perpendicular to the plane to obtain 3D structures. In this case, the calculation method of the fractal dimension in 3D models is $D' = D + 1$. Therefore, the fractal dimensions of models I, II and III are 2.721, 2.674 and 2.593, respectively.

Considering that physisorption is the main form of shale gas adsorption[45], we chose coarse-grained LJ particles instead of a full-atom model to reduce the amount of calculation. In addition, the chemical potential of the simulation cell and fictitious gas reservoir is equal in GCMC simulation. The chemical potential μ of the fictitious gas reservoir is defined as follows[46]:

$$\mu = k_{\text{B}} T \ln \frac{f \Lambda^3}{k_{\text{B}} T}, \tag{13}$$

where f is the fugacity and the thermal de Broglie wavelength $\Lambda = \sqrt{h^2/(2\pi m k_{\text{B}} T)}$, m is the mass of the exchanged particle.

As a real gas rather than an ideal gas, shale gas can be described by the virial equation[47], which reflects the interaction between molecules as it is derived directly from statistical mechanics:

$$Z = \frac{pV}{N k_{\text{B}} T} = 1 + ap + bp^2 + \cdots, \tag{14}$$

where Z is the compressibility factor, p is the pressure, N is the number of molecules, a is the second virial coefficient and b is the third virial coefficient. To obtain the virial coefficients of CH_4 at different temperatures, we first perform MD simulations to calculate the volume of CH_4 at different pressures and then obtain the virial coefficients by fitting the results as shown in Supplementary Fig. S2. By introducing the virial coefficients into equation (14), the compressibility factors under different conditions are obtained (Fig. 5c). In Fig. 5b, for ideal gas, the compressibility factor is $Z = 1$. When attractive forces dominate, $Z < 1$. When the molecules are closer, the repulsive force dominates, making $Z > 1$. The specific values of the virial coefficients of CH_4 at different temperatures are shown in Table 1. The second and third virial coefficients represent the bimolecular attraction and trimolecular repulsion, respectively. The

8

results reveal that the interaction decreases with increasing temperatures. After obtaining the virial

coefficients, the fugacity coefficient φ can be calculated by

$$\varphi = \exp\left(ap + \frac{1}{2}bp^2 + \cdots \right). \tag{15}$$

The fugacity coefficients results for different temperatures and pressures are shown in Fig. 5d.

All these outcomes agree well with the experimental results. Therefore, the obtained virial

coefficients can be used in subsequent studies to convert fugacity to pressure.

This study is to explore the general properties of shale gas through *in situ* simulation. Hence,

we only select shale samples from one representative area (a depth of 2650 m in the Chang 7 shale

of Yanchang formation, Huanxian-Shangliyuan area, Ordos Basin, China) for modeling. There

may be some slight differences for shale gas in other geological regions. Even so, for shale gas in

other geological regions, *in situ* simulations can be established by the above methods.

3.4. Adsorption Isotherms of CH$_4$ in *in situ* Pore Structure. The GCMC simulations were

performed to predict the CH$_4$ adsorption isotherm in three types of *in situ* pore structure at 300 K,

320 K, 340 K and 360 K in fugacity from 0.1 MPa to 36.5 MPa. Here, what we directly count

from the simulation is all the gas molecules in the pores, i.e., the GIP content of the *in situ* pore

structure as shown in Fig. 6a. Conceptually, the GIP content is the sum of absolute adsorbed

amount n_a and free gas amount n_f :

$$n_{GIP} = n_a + n_f = n_a + \frac{pV_f}{k_B T\left(1 + ap + bp^2\right)}, \tag{16}$$

where V_f is the volume of free gas in pores. Additionally, the GIP content consists of excess

adsorbed amount and bulk phase density ρ_g multiplied by the volume of the whole pore V.

Excess adsorbed amount can be obtained by the Gibbs equation:

$$n_e = n_a - \left(V - V_f\right) \cdot \rho_g = n_a - \frac{p\left(V - V_f\right)}{k_B T\left(1 + ap + bp^2\right)}. \tag{17}$$

Combining equations (16) and (17), we obtain the relationship between excess adsorption and

GIP content as follows:

$$n_e = n_{GIP} - \frac{pV}{k_B T\left(1 + ap + bp^2\right)}. \tag{18}$$

Absolute adsorption and excess adsorption models are presented in Figs. 6b,c, respectively.

9

Different from equation (16), V is a constant value that can be determined directly by geometric properties, and V_f is a constant related to geometry, adsorbate and adsorbent properties, which cannot be obtained directly. Therefore, according to the GIP content of models I, II and III (Figs. 6d-f, respectively) we can directly obtain the amount of excess adsorption from equation (18) as shown in Figs. 6g-i. These isotherms reveal that the excess adsorption capacity first increases with the increase in pressure, reaches the maximum adsorption capacity, then decreases, and subsequently increases again after entering ultrahigh pressure. In our simulations, for model I, the pore width is mostly $1 \sim 4.5 \, \text{nm}$, and micropores ($< 2 \, \text{nm}$) account for the majority of pores. Model II mainly contains $1 \sim 6 \, \text{nm}$ wide pores and mesopores ($\geq 2 \, \text{nm}$) account for the majority. In model III, the pore width is mainly $1 : 6 \, \text{nm}$; both micropores and mesopores are present in approximately equal proportions. Obviously, the higher that the temperature is, the lower the maximum adsorption capacity and the higher the pressure required to reach the maximum adsorption capacity. In addition, the pressure required to reach the maximum adsorption is $8 \sim 15 \, \text{MPa}$, which is in good agreement with experimental results[6].

There is an approximate linear decline in the Gibbs excess adsorption isotherm, in which the pressure is approximately $15 \sim 25 \, \text{MPa}$. The compressibility factor Z_a is approximately unchanged in this range (Fig. 5c). Therefore, equation (17) can be transformed into the following form：

$$n_e = n_a + kp , \tag{19}$$

where k is the slope of the excess adsorption isotherm at $15 \sim 25 \, \text{MPa}$, as shown in Supplementary Fig. S3. Thus, we have $k = -(V - V_f)/(k_B T Z_a)$. Because the lower that the temperature and the smaller the compressibility factor, the larger the absolute value of slope, the excess adsorption decreases faster with the increase in pressure. Physically, as pressure increases, the content of bulk molecules increases faster at lower temperatures, resulting in the faster reduction of excess adsorption sites. Therefore, after maximum excess adsorption, the isotherms decrease with the increase in pressure and cross at one point. Beyond that point, the higher that the temperature is, the more the excess adsorption, which is consistent with experimental observations[6].

In addition, the absolute adsorption can be calculated as follows:

$$n_a = n_e + \frac{pkZ_a}{1 + ap + bp^2} \, . \tag{20}$$

According to equation (20), the absolute adsorption isotherms are as shown in Figs. 7d-f. It can be observed that the absolute adsorption isotherm can be divided into three stages. In the first stage, the absolute adsorption increases with increasing pressure due to the existence of a large number of adsorption vacancies. In the second stage, the excess adsorption capacity gradually decreases since the bulk phase occupies a large number of adsorption sites. However, the bulk phase continues to increase, and subsequently, the absolute adsorption capacity remains unchanged due to the offset of the two phases. In the third stage, under the condition of ultrahigh pressure, the absolute adsorption continues to increase primarily as a result of the increase of the bulk phase. Figs. 7a-c present the gas states in the pores at different pressures in the three configurations at 300 K. From left to right, the fugacity is 1 MPa, 6 MPa, 12 MPa and 36 MPa, respectively. At low pressure, the adsorption phase and the bulk phase can be clearly distinguished, and the gas is more easily adsorbed in the smaller pores. With the increase in pressure, the molecule enters the supercritical state, and the proportion of bulk molecules that occupy absolute adsorption sites gradually increases. Until ultrahigh pressure, bulk molecules occupy most of the excess adsorption sites. At this time, the densities of the adsorption phase and the bulk phase are nearly equal.

Previous studies have demonstrated that the larger that the fractal dimensions of the adsorbent surface are, the stronger the adsorption capacity[48]. In this case, although the fractal dimension of model II is larger than that of model III, the adsorption capacity of model III is still larger than that of model II because model II is mainly mesoporous, while model III contains not only mesopores but also micropores. It is certain that the smaller the pore size and the larger the edge fractal dimension, the greater the absolute adsorption capacity is. However, the quantitative relationship between the coupling effect of the fractal dimension and pore size on adsorption capacity requires further study.

3.5. Ultrahigh Pressure Dual-Site Langmuir Adsorption Model. As shown in Fig. 6g, the results of excess adsorption in the kerogen pore model (model I) is in good agreement with experimental results[6]. In their work, the dual-site Langmuir adsorption model was used to fit the experimental results. However, we find that the dual-site Langmuir equation fits well only when

the pressure is below 30 MPa, as shown in Fig. 8a. In addition, the pressure of most shale is higher than 30 MPa. Therefore, it is necessary to modify the original adsorption equation to describe high pressure or even ultrahigh pressure adsorption.

From the analysis of the compressibility factor in the previous section, it can be seen that as the pressure increases, the compressibility factor decreases from 1 and then increases to greater than 1, which reflects the interaction between molecules from no attraction to rejection. When the free molecules are attractive to the adsorbed molecules ($Z < 1$), the adsorption is weakened, and when the free molecules have a repulsive force on the adsorbed molecules ($Z > 1$), it is equivalent to pressing the adsorbed molecules on the substrate, thereby enhancing the adsorption. Therefore, we introduce the compressibility factor to modify the adsorption equation, and the ultrahigh pressure adsorption equation is as follows:

$$n_e(p,T) = \left(n_{max} - V_{max} \cdot \rho_g\right) \cdot \left[(1-\alpha)\left(\frac{K_1(T)p}{1+K_1(T)p}\right) + \alpha\left(\frac{K_2(T)p}{1+K_2(T)p}\right)\right] \cdot Z(p,T), \quad (21)$$

where n_{max} is the maximum adsorption capacity, V_{max} is the volume of adsorption phase at maximum adsorption capacity, $K_1(T)$ and $K_2(T)$ are the equilibrium constant of two different adsorption sites, α is the weight coefficient ($0 < \alpha < 1$).The compressibility factor $Z(p,T)$ is obtained from equation (14). We find that equation (21) fits very well from low pressure to ultrahigh pressure as shown in Fig. 8b. The fitting parameters are shown in Table s2 of the supplementary materials. Therefore, the ultrahigh pressure dual-site Langmuir equation can be used to describe the ultrahigh pressure adsorption on heterogeneous surface. Similarly, the ultrahigh pressure Langmuir equation for molecular adsorption on homogeneous surface can be expressed as follows:

$$n_e(p,T) = \left(n_{max} - V_{max} \cdot \rho_g\right) \cdot \left(\frac{K(T)p}{1+K(T)p}\right) \cdot Z(p,T), \quad (22)$$

where $K(T)$ is the equilibrium constant of single-site.

3.6. Desorption Isotherms of CH$_4$ in *in situ* Pore Structure. We simulated the desorption process of CH$_4$ at different temperatures (i.e., 150 K, 180 K, 210 K, 300 K, 320 K, 340 K and 360 K) in the three *in situ* pore models. Figs. 9a-c present the adsorption and desorption isotherms of CH$_4$ in model I at 150 K, 180 K and 210 K, respectively. When the temperature is below the

critical temperature, desorption hysteresis exists. The hysteresis becomes less obvious as the temperature increases. The appearance of desorption hysteresis is due to the capillary condensation of CH_4 in nanopores. When the temperature is above the critical temperature, no matter how high the temperature is, it cannot liquefy the gas but instead causes it to enter the supercritical state. The critical temperature and pressure of methane are 190.55 K and 4.59 MPa, respectively[49]. Thus, there is almost no desorption hysteresis at 210 K and 300 K (Figs. 9c-f). The desorption isotherms at 320 K, 340 K and 360 K are shown in Supplementary Fig. S4.

To understand capillary condensation on the atomic level, we present a microscopic picture of CH_4 adsorption in nanopores (model I) at low temperature (180 K). Figs. 10a-c present the adsorption of CH_4 at 0.3 MPa, 1 MPa and 2.5 MPa, respectively. Under these conditions, CH_4 should be gaseous. However, the presence of micropores causes the gas to condense into the liquid. The adsorption interface is concave. The saturated vapor pressure of a concave hydraulic surface (p_r) is less than that of flat liquid (p), and the smaller that the pore size is, the lower the pressure required for condensation. This phenomenon can be explained by the Kelvin formula[50]: $\ln(p_r/p) = (2\gamma m_{gas})/(\rho k_B T r)$, where γ is the surface tension, and m_{gas} and ρ are the relative molecular mass and density of the gas, respectively. When the surface is concave, i.e., $r < 0$, the saturated vapor pressure is $p_r < p$. Additionally, as the pressure increases, the area of capillary condensation increases. Fig. 10d shows the details of capillary condensation in nanopores with different curvatures. The CH_4 in the smaller pores and near the concave boundary is liquid, and the center of the pore is gaseous, while the molecules adsorbed at the convex interface and the relatively flat interface do not condense into a liquid state. Therefore, the more concave that the interface is, the more likely it is to cause capillary condensation.

In reality, the storage temperature of shale is much higher than the critical temperature. Therefore, the gas in shale is in the supercritical state. To make the results more intuitive, based on the adsorption results of *in situ* pores, the CH_4 distribution was analyzed by the radial distribution function. Fig. 11a shows the radial distribution of CH_4 in model I at 150 K. We can observe that the distribution has three peaks when the pressure is 1.1 MPa, which means that it has short-range ordered distribution, a liquid characteristic. At a low pressure, the adsorbed gas is primarily gaseous with only one peak, as indicated by the black dot in the figures. Figs. 11b-d are the results

13

for models I, II and III at 300 K, respectively. At ultrahigh pressure ($>40\,\text{MPa}$), the radial distribution has two peaks, and the second peak is relatively weak, which means that the order of CH_4 in these pores is between the gaseous and liquid states, that is, the supercritical state. Figs. 10e-f show CH_4 in supercritical state (360 K, 6 MPa) in nanopores. It can be seen that the adsorption of molecules on the pore walls in the supercritical state is no longer dominant, and it is difficult to condense. This means that there is no liquid-gas phase transition in the desorption process of supercritical CH_4, and there will be no desorption hysteresis.

4. CONCLUSIONS

The *in situ* pore structures of several shale samples drilled from 2650 m deep under the ground and their fractal characteristics were obtained by SEM observation and through image analysis. We find that the fractal features of such structures in shale exhibit regularity: pores in kerogen > kerogen in clay > pores in minerals > pores in clay. Additionally, the effects of substrate strain (or atomic distribution) and adsorption energy on adsorption capacity were investigated. The compressive strain increases the adsorption capacity, and the tensile strain reduces the adsorption capacity under uniaxial strain condition. These results establish a physical foundation for the construction of a simulation model. For the first time, according to the SEM images of three *in situ* pore structures, the corresponding 3D simulation models were geometrically constructed. We obtained the virial coefficients of CH_4 by MD simulations, and they were in good agreement with our previous experiments. Then, the compressibility factors and fugacity coefficients of CH_4 were calculated.

We investigated the adsorption and desorption progresses of CH_4 in fractal nanopores from negative pressure to ultrahigh pressure (i.e., 0.1 MPa ~ 50 MPa) at different temperatures (i.e., 150 K, 180 K, 210 K, 300 K, 320 K, 340 K and 360 K) using GCMC simulations. The GIP content, excess adsorption and absolute adsorption isotherms were clarified. We found the crossover of excess adsorption isotherms, which was observed in a previous experiment, and its mechanism is the competition between the bulk phase and excess adsorption sites. We find that the adsorption capacity is affected by both pore size and fractal dimension. The smaller pores and larger fractal dimensions result in greater adsorption capacity. In addition, we have obtained an ultrahigh pressure dual-site Langmuir equation and it it can accurately describe observed adsorption isotherms from low pressure to ultrahigh pressure. In desorption processes, the hysteresis loop

14

appears at low temperatures but hardly exists in the supercritical state. This phenomenon is due to the occurrence of capillary condensation below the critical temperature. When the temperature is above the critical temperature, the supercritical CH_4 does not condense even at very high pressures. The characteristics of supercritical adsorption (two peaks) and capillary condensation (three peaks) of CH_4 in *in situ* pore were clarified by the radial distribution function. Our study determines the adsorption/desorption behaviors of CH_4 under *in situ* conditions of shale and reveals their microscopic mechanism.

REFERENCES

(1) Burnham, A.; Han, J.; Clark, C. E.; Wang, M.; Dunn, J. B.; Palou-Rivera, I. Life-cycle greenhouse gas emissions of shale gas, natural gas, coal, and petroleum. *Environ. Sci. Technol.* **2011**, *46* (2), 619-627.

(2) Curtis, J. B. Fractured shale-gas systems. *AAPG Bull.* **2002**, *86* (11), 1921-1938.

(3) Tomain, J. P. Shale gas and clean energy policy. *Case W. Res. L. Rev.* **2012**, *63*, 1187.

(4) Howarth, R. W.; Ingraffea, A.; Engelder, T. Natural gas: Should fracking stop? *Nature* **2011**, *477* (7364), 271-275.

(5) Hughes, J. D. Energy: A reality check on the shale revolution. *Nature* **2013**, *494* (7437), 307-308.

(6) Tang, X.; Ripepi, N.; Stadie, N. P.; Yu, L.; Hall, M. R. A dual-site Langmuir equation for accurate estimation of high pressure deep shale gas resources. *Fuel* **2016**, *185*, 10-17.

(7) Wang, Q.; Chen, X.; Jha, A. N.; Rogers, H. Natural gas from shale formation – The evolution, evidences and challenges of shale gas revolution in United States. *Renewable Sustainable Energy Rev.* **2014**, *30*, 1-28.

(8) Chareonsuppanimit, P.; Mohammad, S. A.; Robinson, R. L.; Gasem, K. A. High-pressure adsorption of gases on shales: measurements and modeling. *Int. J. Coal Geol.* **2012**, *95*, 34-46.

(9) Ross, D. J.; Bustin, R. M. Shale gas potential of the lower Jurassic Gordondale member, northeastern British Columbia, Canada. *B. Can. Petrol. Geol.* **2007**, *55* (1), 51-75.

(10) Das, J. Extracting natural gas through desorption in shale reservoirs. *SPE-0112-011-TWA* **2012**, *08* (01), 11-13.

(11) Zeng, W.-T.; Zhang, J.-C.; Ding, W.-L.; Wang, X.; Zhu, D.; Liu, Z. The gas content of continental Yanchang shale and its main controlling factors: A case study of Liuping-171 well in Ordos Basin. *Nat. Gas Geosci.* **2014**, *25* (2), 291-301.

(12) Heller, R.; Zoback, M. Adsorption of methane and carbon dioxide on gas shale and pure mineral samples. *J. Unconv. Oil Gas Resour.* **2014**, *8*, 14-24.

(13) Al Hinai, A.; Rezaee, R.; Esteban, L.; Labani, M. Comparisons of pore size distribution: A case from the Western Australian gas shale formations. *J. Unconv. Oil Gas Resour.* **2014**, *8*, 1-13.

(14) Javadpour, F. Nanopores and apparent permeability of gas flow in mudrocks (shales and siltstone). *J. Can. Pet. Technol.* **2009**, *48* (08), 16-21.

(15) Huang, X.; Zhao, Y.-P. Characterization of pore structure, gas adsorption, and spontaneous imbibition in shale gas reservoirs. *J. Pet. Sci. Eng.* **2017**, *159*, 197-204.

(16) Roychaudhuri, B.; Tsotsis, T. T.; Jessen, K. An experimental investigation of spontaneous imbibition in gas shales. *J. Pet. Sci. Eng.* **2013**, *111*, 87-97.

(17) Liu, K.; Ostadhassan, M.; Gentzis, T.; Fowler, H. Image analysis of the pore structures: An intensive study for Middle Bakken. J. Nat. Gas Sci. Eng. **2019**, 61, 32-45.

(18) Wang, X. H.; Huang, X. F.; Lin, K.; Zhao, Y.-P. The constructions and pyrolysis of 3D kerogen macromolecular models: Experiments and simulations. *Global Challenges* **2019**, *3(5)*, 1900006.

(19) Yang, J.; Hatcherian, J.; Hackley, P. C.; Pomerantz, A. E. Nanoscale geochemical and geomechanical characterization of organic matter in shale. *Nat. Commun.* **2017**, *8* (1), 2179.

(20) Lin, K.; Yuan, Q.; Zhao, Y.-P. Using graphene to simplify the adsorption of methane on shale in MD simulations. *Comput. Mater. Sci.* **2017**, *133*, 99-107.

(21) Mosher, K.; He, J.; Liu, Y.; Rupp, E.; Wilcox, J. Molecular simulation of methane adsorption in micro-and mesoporous carbons with applications to coal and gas shale systems. *Int. J. Coal Geol.* **2013**, *109*, 36-44.
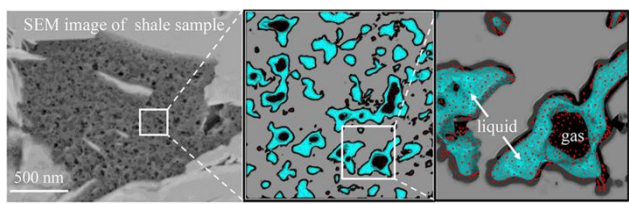
16

(22) Wang, S.; Feng, Q.; Zha, M.; Javadpour, F.; Hu, Q. Supercritical methane diffusion in shale nanopores: effects of pressure, mineral types, and moisture content. *Energy Fuels* **2017**, *32* (1), 169-180.

(23) Chen, C.; Hu, W.; Sun, J.; Li, W.; Song, Y. CH4 adsorption and diffusion in shale pores from molecular simulation and a model for CH4 adsorption in shale matrix. *Int. J. Heat Mass Transf.* **2019**, *141*, 367-378.

(24) Lin, K.; Yuan, Q. Z.; Zhao, Y.-P.; Cheng, C. M. Which is the most efficient candidate for the recovery of confined methane: Water, carbon dioxide or nitrogen? *Extreme Mech. Lett.* **2016**, *9*, 127-138.

(25) Akbarzadeh, H.; Abbaspour, M.; Salemi, S.; Akbari, M. Injection of mixture of shale gases in a nanoscale pore of graphite and their displacement by CO_2/N_2 gases using molecular dynamics study. *J. Mol. Liq.* **2017**, *248*, 439-446.

(26) Su, Y.; Wang, H.; Sheng, G.; Wang, W.; Zhang, Q.; Zhan, S. A model for gas transport in organic matter with isolated pores in shale gas reservoirs. *J. Nat. Gas Sci. Eng.* **2018**, *57*, 178-188.

(27) Zavala-Araiza, D.; Alvarez, R. A.; Lyon, D. R.; Allen, D. T.; Marchese, A. J.; Zimmerle, D. J.; Hamburg, S. P. Super-emitters in natural gas infrastructure are caused by abnormal process conditions. *Nat. Commun.* **2017**, *8*, 14012.

(28) Yu, H.; Zhu, Y.; Jin, X.; Liu, H.; Wu, H. A. Multiscale simulations of shale gas transport in micro/nano-porous shale matrix considering pore structure influence. *J. Nat. Gas Sci. Eng.* **2019**, *64*, 28-40.

(29) Tang, X.; Ripepi, N.; Stadie, N. P.; Yu, L. Thermodynamic analysis of high pressure methane adsorption in Longmaxi shale. *Fuel* **2017**, *193*, 411-418.

(30) Yuan, Q.; Zhu, X. Y.; Lin, K.; Zhao, Y.-P. Molecular dynamics simulations of the enhanced recovery of confined methane with carbon dioxide. *Phys. Chem. Chem. Phys.* **2015**, *17* (47), 31887-31893.

(31) Wu, H. A.; Chen, J.; Liu, H. Molecular Dynamics Simulations about Adsorption and Displacement of Methane in Carbon Nanochannels. *J. Phys. Chem. C* **2015**, *199*, 13652-13657.

(32) Liu, Y.; Wilcox, J. Effects of surface heterogeneity on the adsorption of CO_2 in microporous carbons. *Environ. Sci. Technol.* **2012**, *46* (3), 1940-1947.

(33) Wang, M.; Xue, H.; Tian, S.; Wilkins, R. W.; Wang, Z. Fractal characteristics of Upper Cretaceous lacustrine shale from the Songliao Basin, NE China. *Mar. Pet. Geol.* **2015**, *67*, 144-153.

(34) Liu, X.; Nie, B. Fractal characteristics of coal samples utilizing image analysis and gas adsorption. *Fuel* **2016**, *182*, 314-322.

(35) Yang, F.; Ning, Z.; Liu, H. Fractal characteristics of shales from a shale gas reservoir in the Sichuan Basin, China. *Fuel* **2014**, *115*, 378-384.

(36) Clarkson, C. R.; Solano, N.; Bustin, R. M.; Bustin, A. M. M.; Chalmers, G. R. L.; He, L.; Melnichenko, Y. B.; Radliński, A. P.; Blach, T. P. Pore structure characterization of North American shale gas reservoirs using USANS/SANS, gas adsorption, and mercury intrusion. *Fuel* **2013**, *103*, 606-616.

(37) Cui, J. W.; Zhu, R. K.; Fan, C. Y.; Li, S. X.; Mao, Z. G.; Li, S.; Zhang, Z. Y. Oil and gas resources of shale formation orderly accumulation and coexistence as well as its prospecting significance: A case study of Chang 7 shale formation in Ordos Basin. *Geological Bulletin of China*, **2019**, *38* (6), 1052-1061. (in Chinese with English abstract)

17

(38) Ju, W.; You, Y.; Chen, Y.; Feng, S.; Xu, H.; Zhao, Y.; Liu, B. Nanoscale pore structure and fractal characteristics of the continental Yanchang formation Chang 7 shale in the southwestern Ordos Basin, central China. *Energy Sci. Eng.* **2019**, *7*, 1188-1200.

(39) Plimpton, S. Fast Parallel Algorithms for Short-Range Molecular Dynamics. *J. Comput. Phys.* **1995**, *117* (1), 1-19.

(40) Lennard-Jones, J. E.; Devonshire, A. Critical phenomena in gases-I. *Proc. R. Soc. Lond. A Mat.* **1937**, *163* (912), 53-70.

(41) Dauber-Osguthorpe, P.; Roberts, V. A.; Osguthorpe, D. J.; Wolff, J.; Genest, M.; Hagler, A. T. Structure and energetics of ligand binding to proteins: Escherichia coli dihydrofolate reductase-trimethoprim, a drug-receptor system. *Proteins* **1988**, *4* (1), 31-47.

(42) Karniadakis, G. E.; Beskok, A.; Aluru, N. *Microflows and nanoflows: fundamentals and simulation*. Springer Science & Business Media: 2006; Vol. 29.

(43) Theiler, J. Estimating fractal dimension. *J. Opt. Soc. Am. A* **1990**, *7* (6), 1055-1073.

(44) Ericksen, J. L. On the Cauchy-Born rule. *Math. Mech. Solids* **2008**, *13* (3-4), 199-220.

(45) Kurniawan, Y.; Bhatia, S. K.; Rudolph, V. Simulation of binary mixture adsorption of methane and CO_2 at supercritical conditions in carbons. *AlChE J.* **2006**, *52* (3), 957-967.

(46) Cracknell, R. F.; Nicholson, D.; Quirke, N. Direct molecular dynamics simulation of flow down a chemical potential gradient in a slit-shaped micropore. *Phys. Rev. Lett.* **1995**, *74* (13), 2463-2466.

(47) Onnes, H. K. In *Expression of the equation of state of gases and liquids by means of series*, KNAW, Proceedings, 1901; pp 125-147.

(48) Sun, W. J.; Feng, Y. Y.; Jiang, C. F.; Chu, W. Fractal characterization and methane adsorption features of coal particles taken from shallow and deep coalmine layers. *Fuel* **2015**, *155*, 7-13.

(49) Sloan Jr, E. D. Fundamental principles and applications of natural gas hydrates. *Nature* **2003**, *426* (6964), 353.

(50) Thomson, W. On the equilibrium of vapour at a curved surface of liquid. *Proc. R. Soc. Edinb.* **1872**, *7*, 63-68.

19

Graphical table of contents

1
2
3
4
5
6
7
8
9
10
11
12
13
14
15
16
17
18
19
20
21
22
23
24
25
26
27
28
29
30
31
32
33
34
35
36
37
38
39
40
41
42
43
44
45
46
47
48
49
50
51
52
53
54
55
56
57
58
59
60

Table 1 Second and third virial coefficients of CH$_4$ at different temperatures.

Temperature (K)	Second virial coefficient (MPa^{-1})	Third virial coefficient (MPa^{-2})
300	-0.01689	4.33309×10^{-4}
320	-0.01508	4.04940×10^{-4}
340	-0.01209	3.41599×10^{-4}
360	-0.01017	3.06301×10^{-4}

21
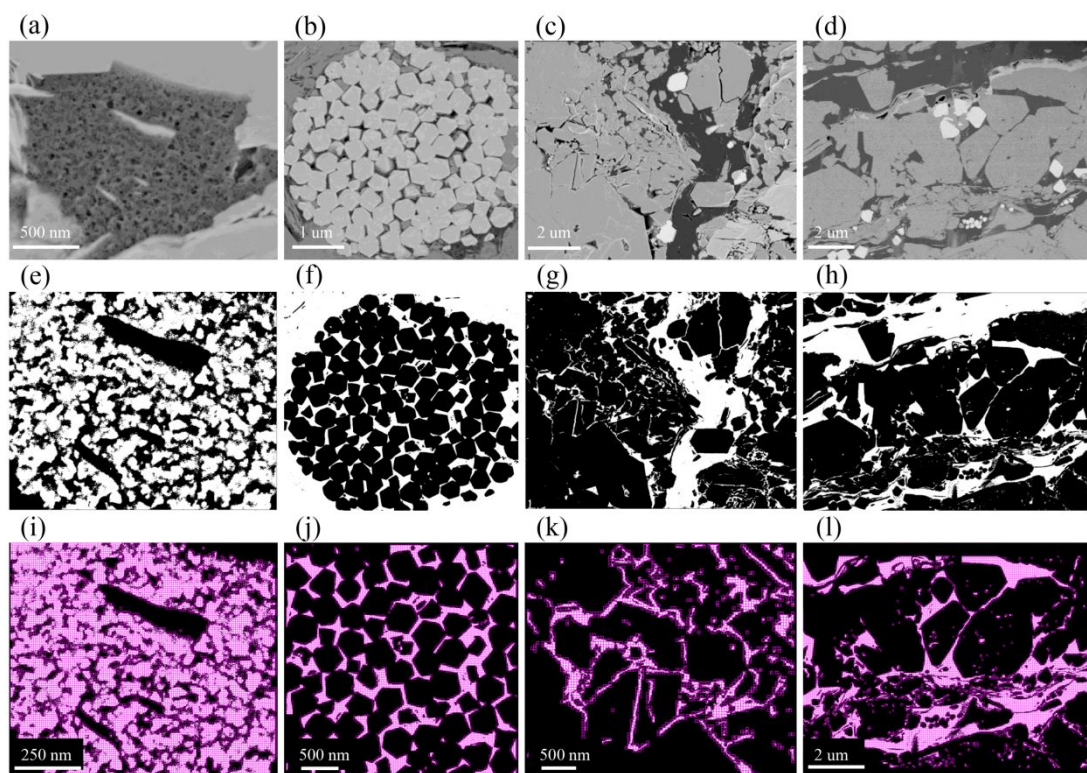
Figure 1. Box-counting method procedure for fractal dimension *D* of shale samples. (a-d) SEM images of shale, (a) Pores in kerogen, (b) Pores in minerals, (c) Pores in clay and (d) Kerogen in clay. (e-h) Binary images. (i-l) Covering the boxes on the pores.
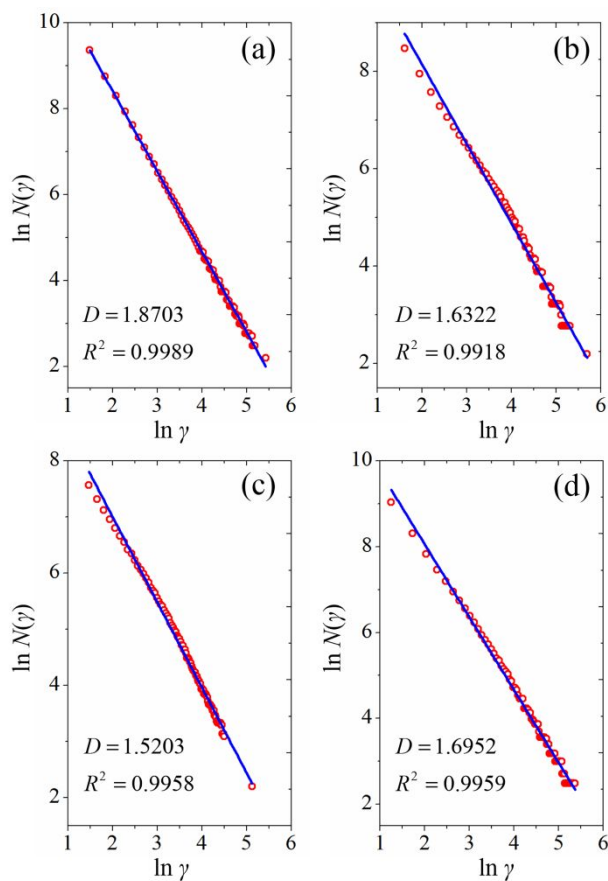
Figure 2. Fractal dimension calculation results from SEM image analysis; red indicates the data point; blue indicates the linear fit line. (a**)** Pores in kerogen, (b) Pores in minerals, (c) Pores in clay and (d) Kerogen in clay.

23
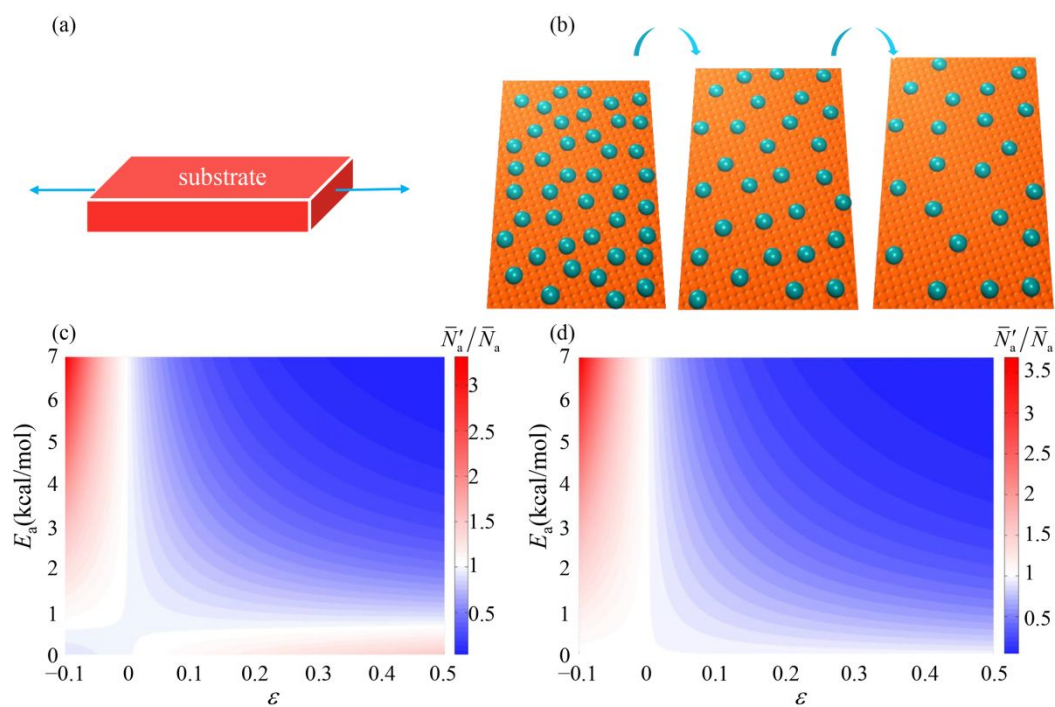
Figure 3. Effect of substrate properties on adsorption. **(**a) Uniaxial strain conditions. (b) Gas desorption due to tensile stain of substrate. (c) Effects of strain and adsorption energy on total adsorption capacity. (d) Effects of strain and adsorption energy on adsorption capacity per unit area.
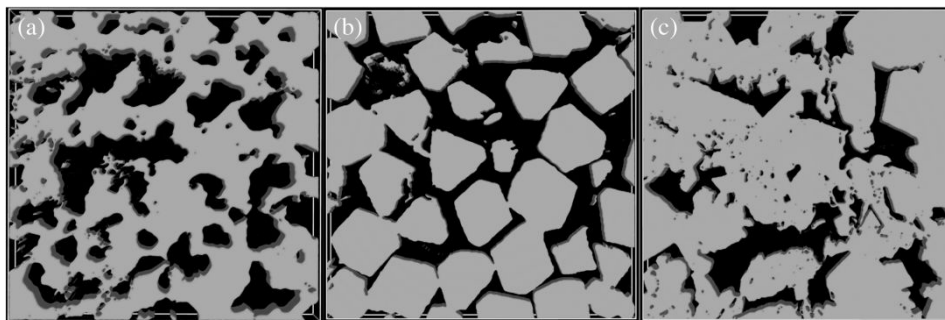
Figure 4. MD simulation models with an *in situ* pore structure. (a) I: Pores in kerogen. (b) II:

Pores in minerals. (c) III: Pores in clay.
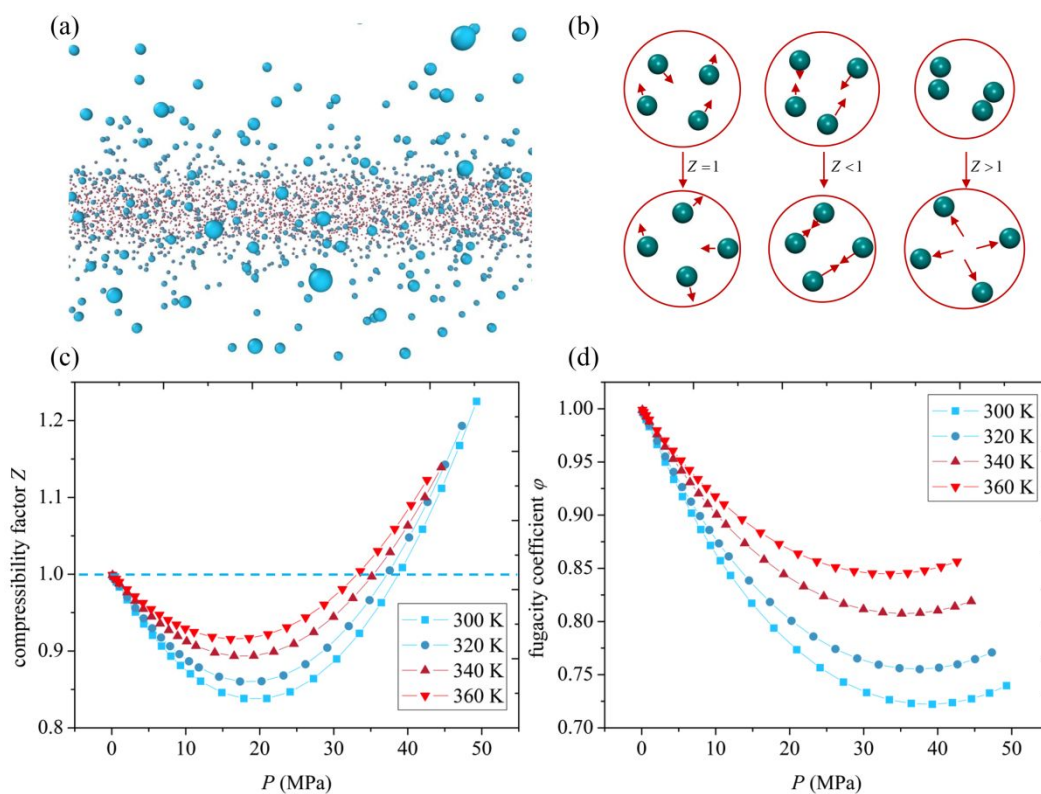
Figure 5. (a) MD simulation of CH$_4$ under high pressure. (b) Interaction of particles under different compressibility factors Z. (c) Compressibility factors of CH$_4$ at different pressures and temperatures. (d) Fugacity coefficients φ of CH$_4$ at different pressures and temperatures.
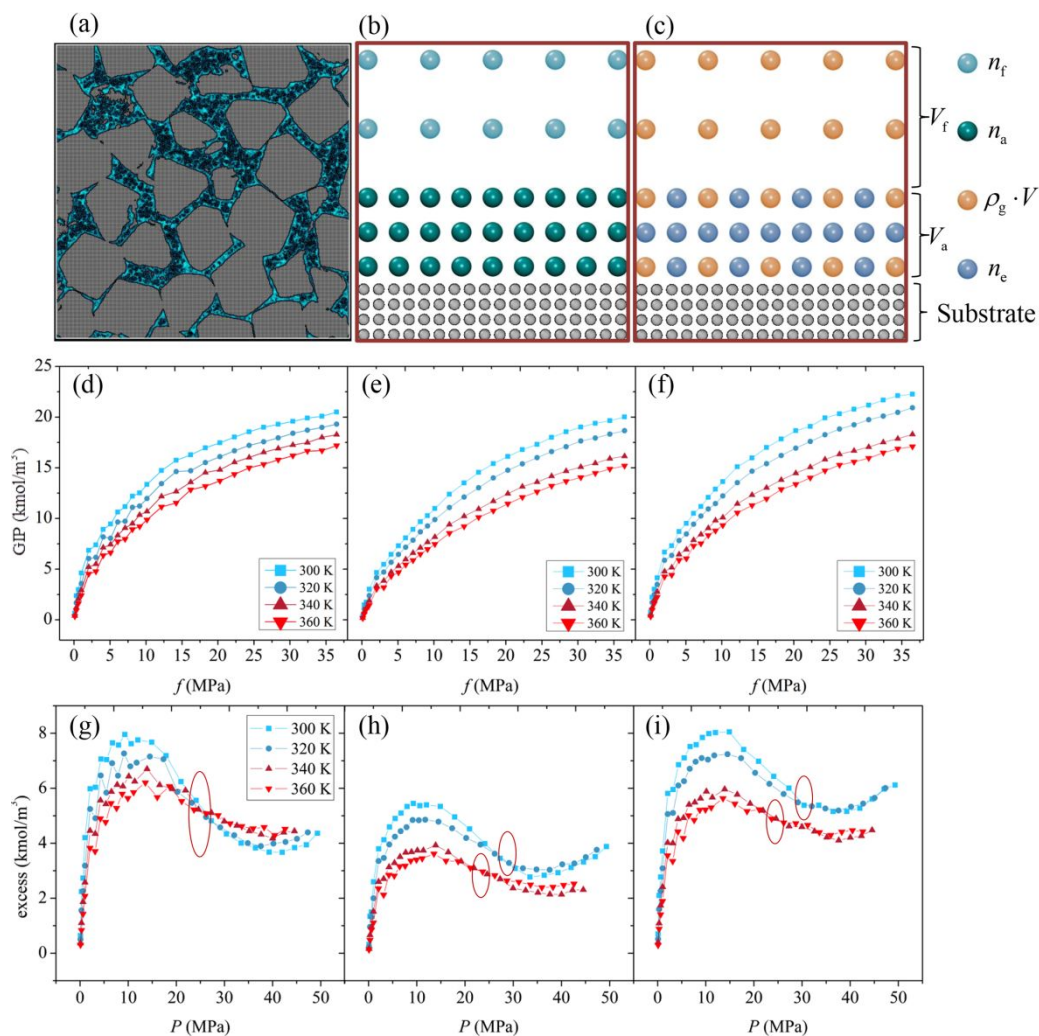
Figure 6. (a) CH_4 adsorbed in porous media. (b) Absolute adsorption model. (c) Excess adsorption model. (d-f) GIP content of CH_4 in models I, II and III. (g-i) Excess adsorption of CH_4 in models I, II and III, respectively.

27
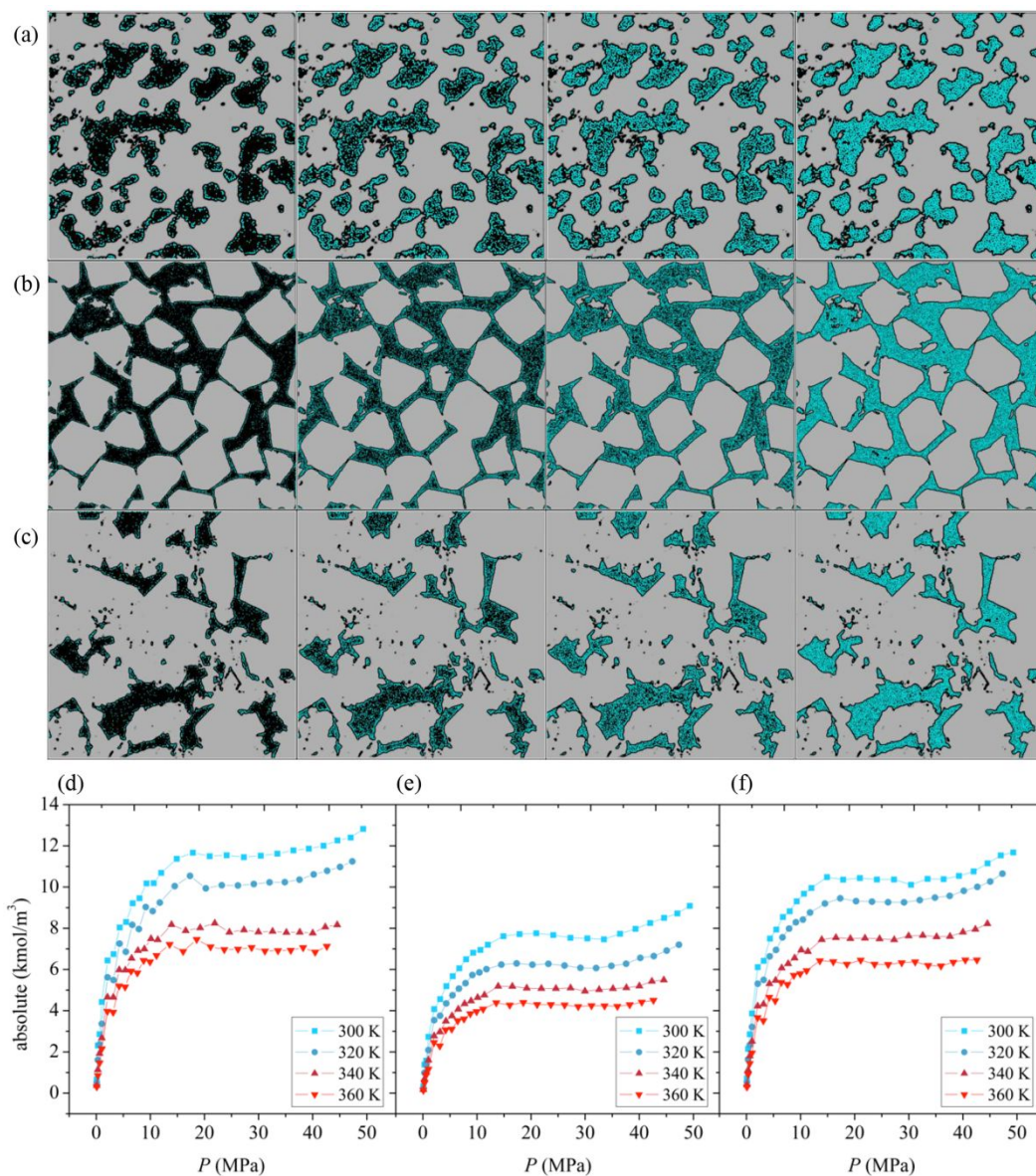
Figure. 7 Adsorption of CH$_4$ in three *in situ* models I (a), II (b) and III (c) at 300 K and fugacity at 1, 6, 12 and 36 MPa, respectively. Absolute adsorption isotherms of CH$_4$ in models I (d), II (e) and III (f).
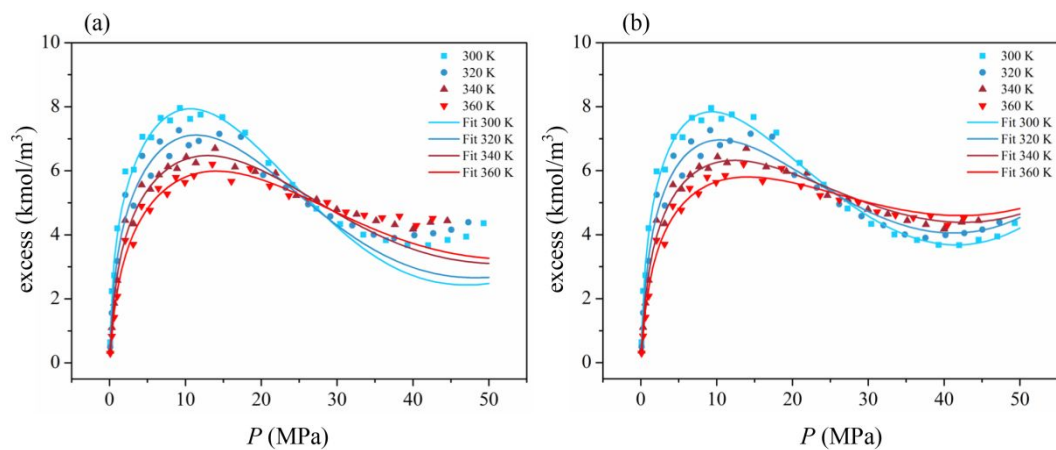
Figure 8. (a) Dual-site Langmuir equation fits *in situ* simulation results. (b) Ultrahigh pressure dual-site Langmuir equation fits *in situ* simulation results.
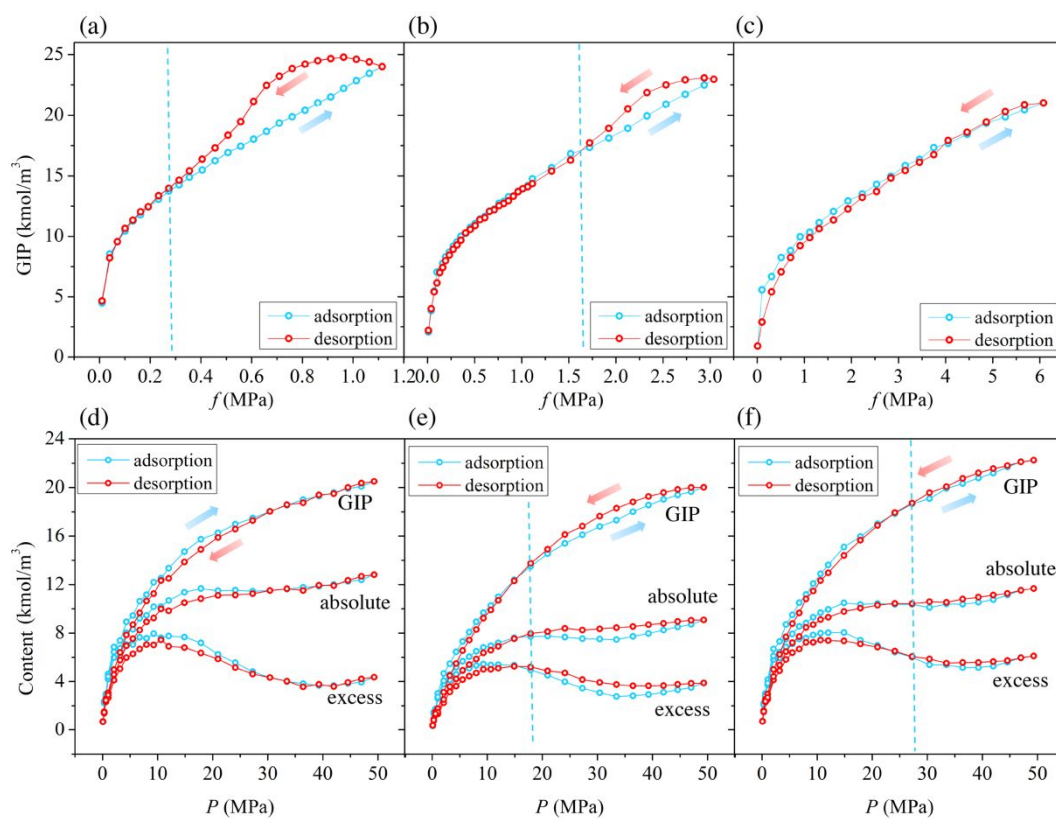
Figure 9. Blue indicates the adsorption isotherm, and red indicates the desorption isotherm. (a), (b) and (c) represent the GIP content of CH_4 in model I at 150 K, 180 K and 210 K, respectively. (d), (e) and (f) represent the GIP content of CH_4 at 300 K in models I, II and III, respectively.
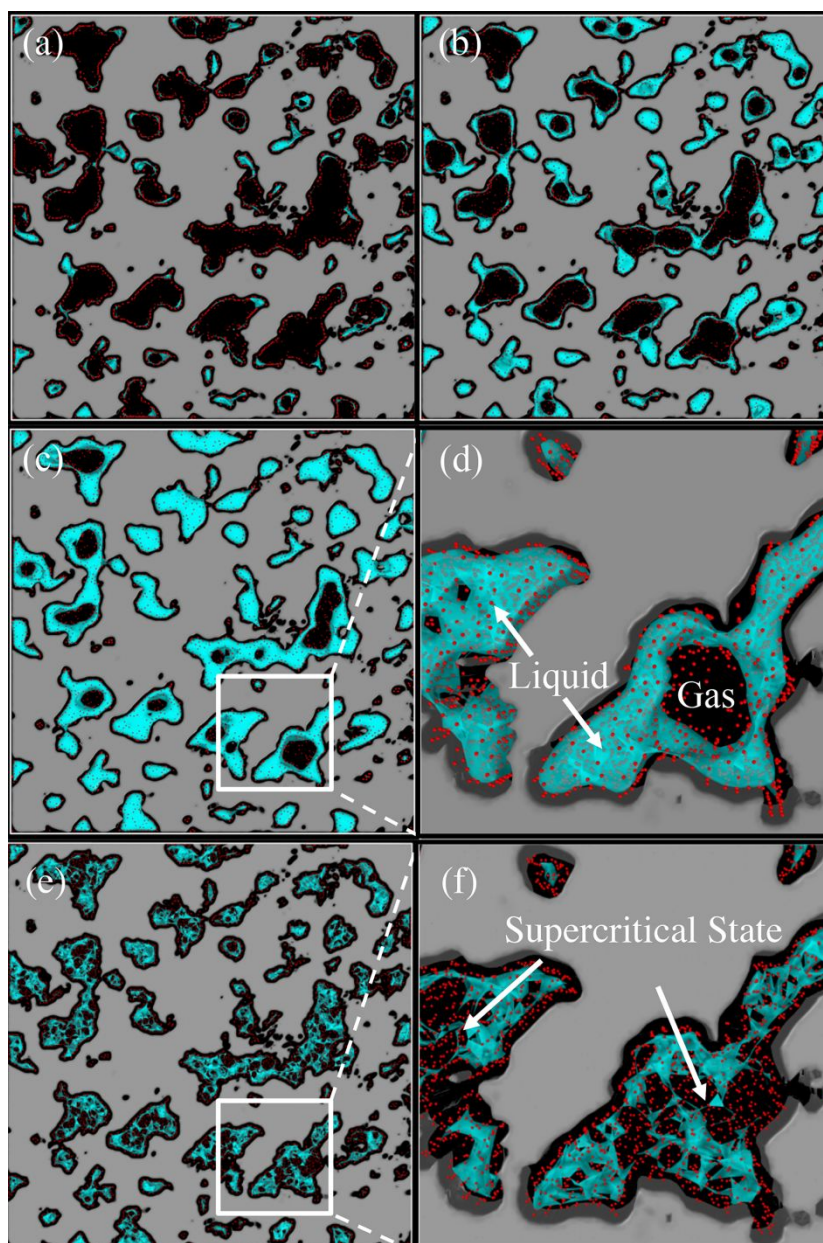
Figure 10. Capillary condensation of CH_4 in pores under different pressures: (a) 0.3 MPa, (b) 1 MPa, (c) 2.5 MPa, (d) Details of CH_4 storage in nanopores; (e-f) Supercritical CH_4 in pores at 360 K and 6 MPa.
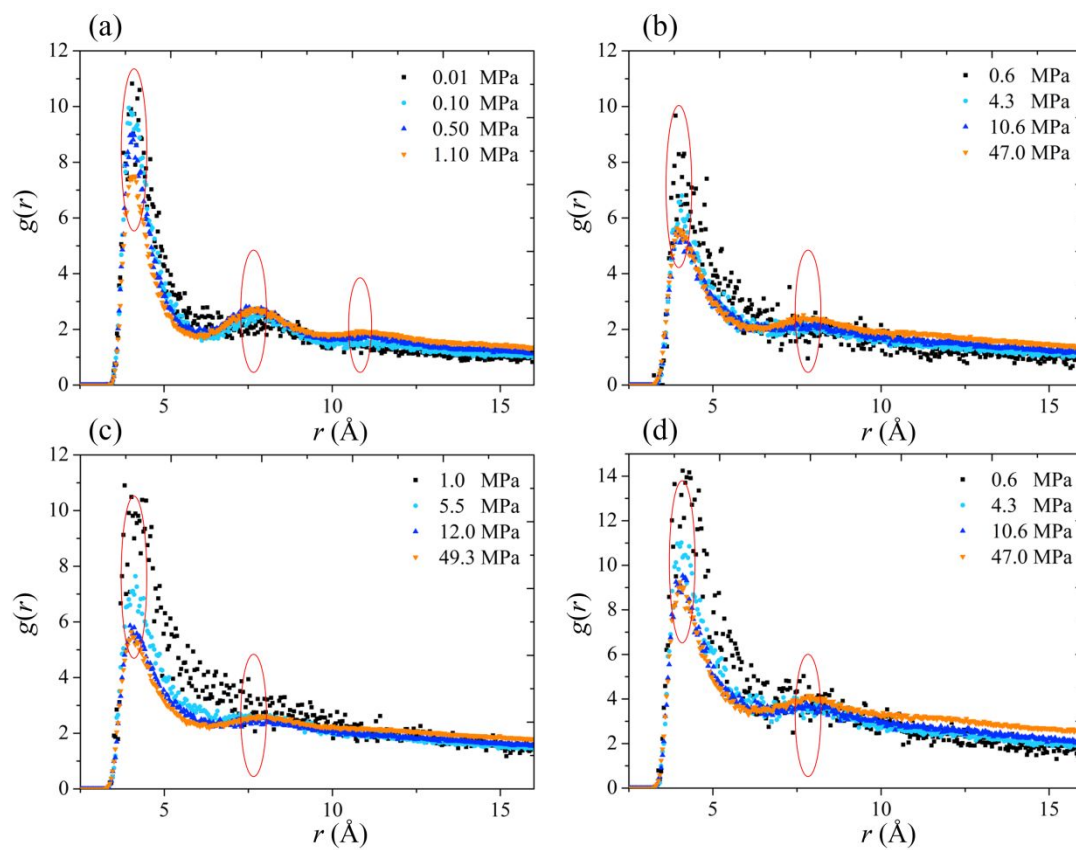
Figure 11. Radial distribution functions $g(r)$. (a) At 150 K in model I. (b) At 300 K in model I.

(c) At 300 K in model II. (d) At 300 K in model III.